Heliyon 9 (2023) e19623

Contents lists available at ScienceDirect

Heliyon

journal homepage: www.cell.com/heliyon

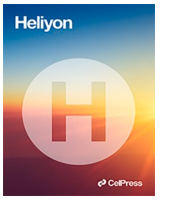

Hydrodynamic performance assessment of photocatalytic reactor with baffles and roughness in the flow path: A modelling approach with experimental validation

M.G. Rasul [a,*], S. Ahmed [a], M.A. Sattar [a,b], M.I. Jahirul [a]

[a] School of Engineering and Technology, Central Queensland University, Rockhampton, Queensland, 4702, Australia
[b] Mechanical and Product Design Engineering, Swinburne University of Technology, Hawthorn, 3122, Australia

ARTICLE INFO

Keywords:
Flat plate photocatalytic reactor
Hydrodynamic performance assessment
Modelling
Formic acid flow phenomena
Baffles and roughness in flow path

ABSTRACT

Purification of wastewater is essential for human being as well as for the flora and fauna, and sustainable environment. Photocatalytic reactor with TiO_2 coated layer can be used to degrade the pollutants but without proper pollutant mass transfer in the reactive surface, photocatalytic reactor decreases its effectiveness. The baffles and rough surface in the flow path can improve the fluid mixing to enhance pollutant mass transfer to improve the reactor's performance. In this study, a computational fluid dynamics (CFD) model has been developed to investigate the effect of four top baffles and three rough surfaces (semi-circular, triangle, and rectangle) on pressure drops, mass transfer and the hydrodynamic performance of the reactor. The experimental investigation was carried out using Formic Acid (FA) as pollutant in feed water for model validation. The simulated result varies only within 5% with the experimental data of FA concentration versus feed flow rate and fluid velocity. The model was run at fluid velocity of 0.15 m/s and 0.5 m/s (Reynolds number of 2150 (laminar flow) and 7500 (turbulent flow), respectively. The simulation result shows that the addition of baffles and roughness on the reactive surfaces increases the turbulent kinetic energy (minimum increase 8%) and consequently increases the mass transfer (maximum increase 37%) of the pollutant. The highest wall shear was observed to be 40 Pa when both square and triangular elements were used as roughness elements at turbulent flow condition. The results also shows that the highest pressure-drop of 8 kPa was found when the square roughness element was used at turbulent flow condition. Overall, the photocatalytic reactor performance is significantly enhanced by the application of combined baffles and roughness elements in the reactive surface.

1. Introduction

Purification of water is outpost important for the flora and fauna as well as sustainable environment [1,2]. Among available the processes heterogeneous photocatalysis is the most promising technique which does not require chemical to process as well as effective to degrade a wide range of pollutant [1,3,4]. Although photocatalysis has drawn attention of research worldwide because it can use solar energy to solve environmental problems by treating wastewater pollution [5–7], however the photocatalysis needs an appropriate catalyst to be effective to use the solar energy. The design of heterogeneous of photocatalytic reactor is complex and requires

* Corresponding author.
E-mail address: m.rasul@cqu.edu.au (M.G. Rasul).

https://doi.org/10.1016/j.heliyon.2023.e19623
Received 30 March 2023; Received in revised form 9 August 2023; Accepted 28 August 2023
Available online 29 August 2023

understanding of environmental, mechanical, and chemical engineering concepts [8]. Heterogeneous process which uses TiO_2 and UV light for degradation of pollutant has higher efficiency compared to other process [9–12] hence has gained much attention to researchers [13,14]. TiO_2 based photo-anodes has good electrical properties, chemical stability, and light-dependent properties. The cost is low cost, and it has environmental safety for this it is used in photo-electrochemical cells [15–18]. Rathna et al. [19] used nanoparticle to enhance the photocatalytic reactor's performance. They incorporated TiO_2–WO_3 nanoparticles into the Polyaniline polymer matrix and found that the nanoparticle incorporation improves degradation of photocatalytic membrane reactor. Zhuang et al. [20] used carbon nanotube in TiO_2 to enhance its performance. They found that the removal of Hg0, the adsorption and photocatalytic oxidation of the rector have improved. Pei et al. [21] used novel composite nanofibers of TiO_2/ZnO/Bi_2O_3 as photocatalytic reactor for NO and o-xylene degradation using solar radiation and found that the novel composite nanofibers of TiO_2/ZnO/Bi_2O_3 provides better photocatalytic conversion than commercial one for the NO oxidation under the solar irradiation simulated. Riaz and Park [22] has reviewed photocatalytic membrane reactors based on TiO_2 for wastewater and water purification and found that TiO_2 affects the performance of membrane. They also found that the irradiation source and time also affects the performance of the membrane and suggested that the solar light is better than that of the UV light. The performance of the reactor diminishes because the pollutant contact with the reacting surface is hindered by the sediment deposition. Jafarikojour et al. [23] used imping jet to enhance the immobilized photocatalytic reactor performance for the phenol degradation. Their results show that initial phenol concentration, the liquid flow rate, nozzle-to-disc distance, and coating disc diameter affect the degradation and found 79% and 84% removal of TOC and COD respectively. Bai et al. [24] developed a novel dual heterojunction Photocatalytic Fuel Cell system using ZnO/CuO nanowires/FTO photocathode and $BiVO_4$/TiO_2 nano tubes/FTO photoanode to decompose methylene blue, Congo red, and methyl orange. Their novel Photocatalytic Fuel Cell is cost effective and achieved 90%,83%, and 76% degradation of methylene blue, Congo red, and methyl orange respectively after 80 min reaction. Photocatalytic reactor was used by Tahir et al. [25] to convert CO_2 and methane (CH_4) to fuel and suggests that this conversion process is environmentally friendly as it uses light source to convert. Hurtado et al. [26] investigated the effect of silver on the $Li_{1-x}Ag_xVMoO_6$ on the photocatalytic performance and found that the $Li_{1-x}Ag_xVMoO_6$ shows better performance of photocatalytic conversion than that of TiO_2.

Degradation of organic compound depends on many parameters such as light intensity, photocatalyst, initial concentration of substrate etc and a substantial amount of research has been carried out to improve the performance of reactor [27]. Mechanical device such as baffles in an immobilized photocatalytic reactor is used to improve the fluid mixing and pollutant mass transfer on the TiO_2 coated layer [28]. Baffle can effectively change the boundary layers and concentration by producing vortices or creating recirculation zone in the flow field downstream of the baffle [29]. The flow reattachment behind the baffle creates scrubbing effect on the reactive surface and increase in the mass transport rate and contact of pollutant with the reacting surface. Using of baffle and other types of mechanical devices in engineering applications including immobilized photocatalytic reactor to enhance the mass transfer enhancement has been reported by several researchers. The mass transfer enhancement elements such as repeated ribs or delta wing mixer in an immobilized annular reactor enhance the performance of reactor degradation but increase the pressure loss. Several authors investigated the use of internal mechanisms such as baffles and found that the baffles would promote the resistance of mass transfer in an immobilized photocatalytic reactor [30–32]. As per author' knowledge, there are virtually none investigations available in the literature that have considered the mass transfer resistance under the influence of turbulence promoting solid baffles. The pressure drop significantly depends on the height of baffles in the reactor module.

In general, the increase of turbulence using promoter/baffle can increase pressure loss due to increased skin friction. The pressure drop will increase energy consumption therefore the minimization of pressure drop is important to enhance the design and to reduce the operational cost by minimizing the energy. The spacing and height of baffle are deemed to be the most crucial parameters for the improvement of the design of the reactor. The spacing and height of the baffle can affect the mass transfer of the pollutant at the same time it can have an impact on the pressure drop or vice versa. So, the influence of baffle size and shape on the photocatalytic reactor performance are not fully understood for a given configuration. The analysis of the combined influence of baffle and roughness on the performance of photocatalytic reactor are limited in the literature. Optimum baffle design is not available in the current literature but a baffle height of 0.5 and spacing of 2 times of the channel height is studied in many previous works. Lira et al. [33] investigated the performance of a curved channel reactor and considered the effect of Dean flow and analysed the mass transfer characteristics and fluid flow using CFD model. Moreira and Puma [34] investigated an annular photocatalytic reactor performance using CFD model. They used the Six-Flux model (SFM) with isotropic scattering and the Discrete Ordinates Model (DOM) to solve the Radiative Transfer Equation (RTE). They used to model predict the intrinsic reaction kinetics constant of photocatalytic oxidation of water contaminants and found the good agreement with experimental data. Deng et al. [35] simulated the effect of baffles on heterogeneous photocatalytic oxidation of gas-phase ethylene in three annular reactors using computational fluid dynamics. They found that the baffles can improve the uniformity of flow and prolong the residence time.

In this study, a CFD model has been developed and numerical simulation has been conducted to examine the hydrodynamic performance of a photocatalytic reactor with combined baffles and roughness elements in the reactive surface. The model was validated with the experimental data of pollutant concentration as a function of fluid flow rate and fluid velocity with respect to time. Then, the baffles and roughness were added into the numerical models and the performance of the photocatalytic reactor was investigated with roughness and top baffle and compared with the baseline model without baffle and roughness. Several types of roughness were used in the model to examine the influence of the shape on the hydrodynamic performance of the photocatalytic reactor. The combined effect of top baffle and roughness elements was studied to examine their role on the flow and mass transfer pattern while ensuring sufficient mixing to enhance mass transfer. The arrangement of baffle and roughness is designated as combined reactor which is designed to stretch and tilt the flow to increase both the residence time and mixing efficiency of the reactive species in the reactor. In the present study, the numerical simulation was carried out at both low (laminar flow) and high (turbulent flow)

Reynolds number for a range of top baffles fitted on the upper walls and roughness fitted on the bottom wall which is the reactive section of the reactor to get an understanding on the observed flow pattern and mass transfer performance. Although, there are some studies available on the effect of baffle on hydrodynamic performance of photocatalytic reactor, the novelty of this study is the investigation of combined effect of baffles of different shapes and sizes, and roughness elements on the pressure-drop and the hydrodynamic performance of the reactor. The mass transfer and their correlation with the hydrodynamics of the flow is also investigated in this study.

2. Modelling of baffle and roughness in photocatalytic reactor

2.1. Mathematical modelling and governing equations

The governing equation used for the modelling of the photocatalytic reactor is presented and discussed in this section. The fluid was considered as incompressible with constant properties and the fluid flow was assumed to be governed by the Navier–Stokes and the continuity equations. Turbulent flow in the reactive domain containing baffle and roughness elements with the consideration of the species (i.e., formic acid FA) concentration variation was dealt with the time averaged governing flow equations. The concentration field of FA under prevailing hydrodynamics were accounted using a convection-diffusion equation. The turbulent flow was modelled using the RNG k-ε model and enhanced wall treatment (EWT) was incorporated. EWT is a near-wall modelling method in FLUENT software that combined a two-layer model applied in regions with fine near-wall meshes and enhanced wall functions in regions with coarse meshes [36]. It is also essential to employ a fine mesh which will solve the governing equations near to the wall, when modelling turbulent flow using either low Reynolds number turbulence model or enhanced wall treatment. In the present study, at the wall-adjacent cell a y + smaller than 0.5, and at the viscosity-affected near-wall region ($Re_y = 200$) at least 10 cells were defined in all the simulations [37]. Based on the assumptions described above and the RANS turbulence modelling [38], the CFD model solves the continuity Eqn. (1), RANS Eqn. (2) and time-average conservation of species Eqn. (3) by a finite volume technique and the equations can be expressed as:

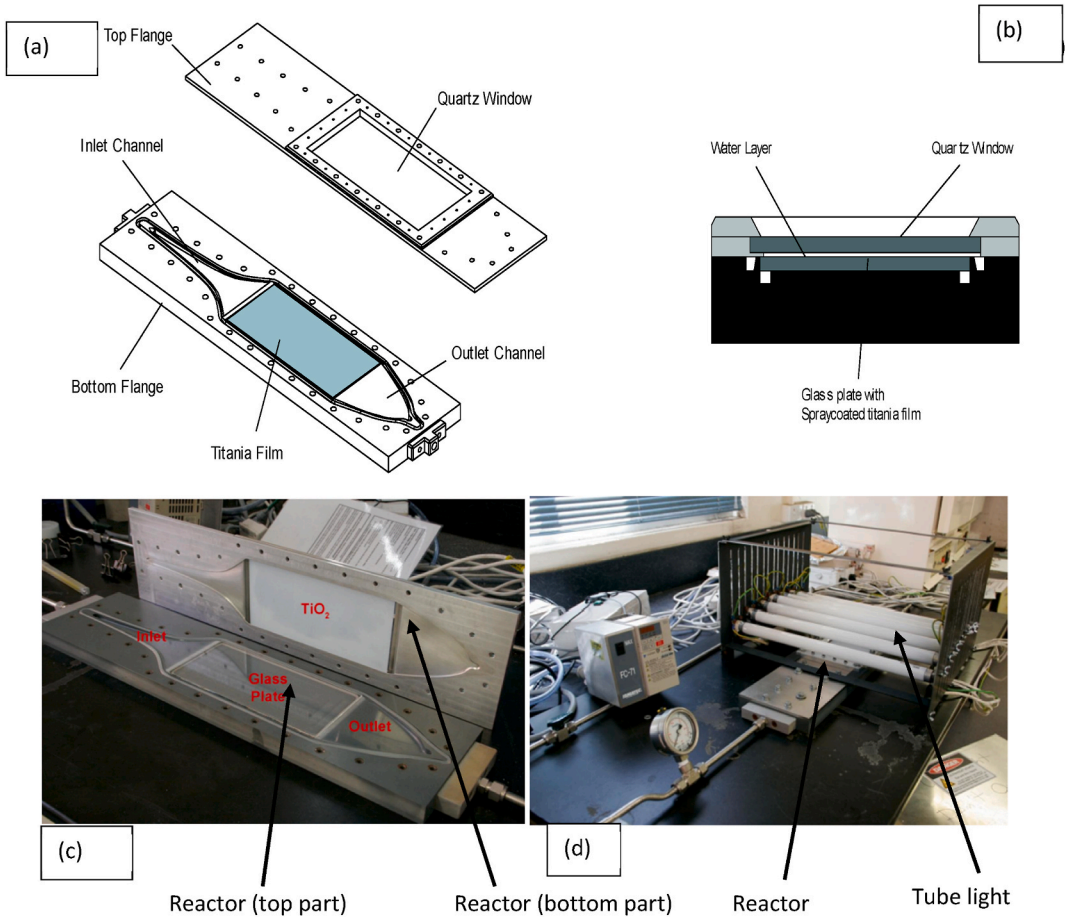

Fig. 1. Schematic of the photocatalytic reactor (a) Top and bottom part; (b) cross section of reactive area and picture of (c) reactor (top and bottom flange) (d) illumination system.

$$\frac{\partial(\rho)}{\partial t} + \nabla.(\rho\overline{u}) = 0 \tag{1}$$

$$\frac{\partial}{\partial t}(\rho\nabla) + \nabla.(\rho\overline{uu}) = -\nabla\overline{P} - \nabla.\tau \tag{2}$$

$$(\rho\overline{U}\overline{m_k} + \rho\overline{um_k} = -\nabla\overline{J_k} \tag{3}$$

In this study, for turbulent flow simulation, the RNG k-ε model employed can be expressed for k and ε transport as:

$$\frac{\partial}{\partial t}(\rho\varepsilon) + \frac{\partial}{\partial x_i}(\rho\varepsilon u_i) = \frac{\partial}{\partial x_j}\left[\left(\mu + \frac{\mu_t}{\sigma_\varepsilon}\right)\frac{\partial\varepsilon}{\partial x_j}\right] + C_{1\varepsilon}\frac{\varepsilon}{k}P_k - C^*_{2\varepsilon}\rho\frac{\varepsilon^2}{k} \tag{4}$$

$$C^*_{2\varepsilon} = C_{2\varepsilon} + \frac{C_\mu\eta^3\left(1 - \frac{\eta}{\eta_0}\right)}{1 + \beta\eta^3} \tag{5}$$

In this model, mean velocity gradient and the Reynolds stresses with turbulent viscosity (μ_t) is related using Boussinesque approximation. In Equations (4) and (5), $P_k = \mu_t S^2$ or $P_k = -\rho\overline{u_i'u_j'}\frac{\partial u_i}{\partial x_i}$ is the turbulent kinetic energy producion term, and S is the strain tensor, where $S = (2S_{ij}S_{ij})^{1/2}$. Using the following equation μ_t the turbulent viscosity is estimated,

$$\mu_t = \rho C_\mu\frac{K^2}{\varepsilon} \tag{6}$$

Here $C_\mu = 0.0845$ and the model constants are: $C_{1\varepsilon} = 1.42$, $C_{2\varepsilon} = 1.68$, $\eta_o = 4.38$ and, $\beta = 0.012$.

2.2. Geometry, meshing and methodology

The schematic of the experimental model is shown in Fig. 1(a)-(b). The numerical model developed for the simulation is same as the reactive section of the experimental model as shown in Fig. 1(b). The picture of the experimental set up designed and built for the experiment is shown in Fig. 1(c)–(d). The H_2O_2 solution was used to degreased glass plate and deionized water was used to cleaned it. For better adhesion, the surface was etched with diluted nitric acid and the surface was cleaned and dried before applying the TiO_2 coating. The solution was prepared by mixing TiO_2 powder with the reagent ethanol and the solution was sonicated for an hour for homogenization. The suspension was agitated using a magnetic stirrer during the coating process. The TiO_2 solution was deposited on the surface using spray coating deposition technique and the surface was dried in an incubator for 2 h. This process was repeated several times to achieve desired thickness. The coated surface was placed inside and oven at 400 °C to stabilize the TiO_2 on the surface. The thickness was measured using scanning electronic microscope (SEM). A total of five coated surface with thickness of approximately 0.52, 1.21, 2.24, 4.77 and 7.01 μm were prepared. Several experiments were carried out to find out the optimum thickness. The experiment was conducted with a thickness of 4.77 μm based on the experimental results obtained.

The main part of the reactor are top and bottom flanges, TiO_2 films and reaction area. The glass was coated with TiO_2 films (220 × 100 × 3.5 mm) and laid on the bottom flange and the upper part has glass windows which allow UV light. An array of tube light was set at the top of the upper glass window. The model was run with irradiance of 70.6, 57.9, 37.1 and 20.4 W m^{-2}. Seven 15 W ultra-violet lamps were used in this experiment whose position can be controlled vertically to change irradiance.

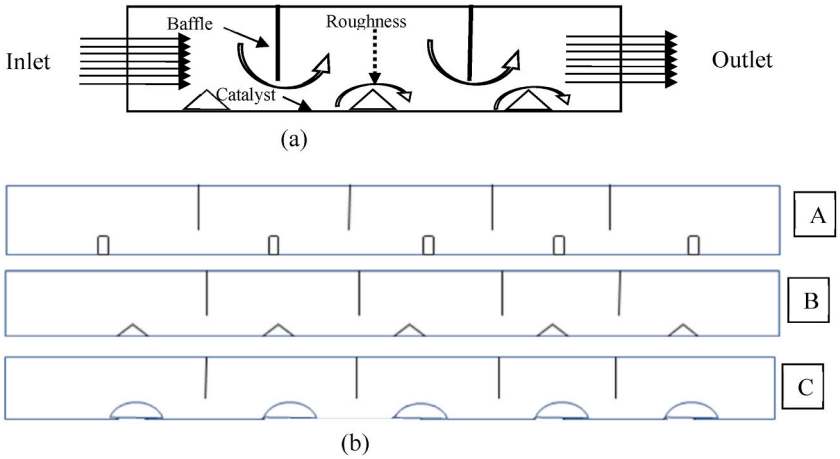

Fig. 2. Schematic diagram of the reactive section (a) equipped with baffle and roughness elements (b) A) square B) triangle, and C) semi-circle.

In the present simulation, a 2D model of the reactor was used for the CFD modelling as presented in Fig. 2. The main parts are reactive area, the inlet, and outlet. A set of top baffles is placed on the upper wall and the roughness elements is on the lower walls which can be seen in Fig. 2. The reactive section was considered 15 mm in height and 200 mm in length where a set of top baffles with 10 mm height and roughness with 1.5 mm height were specified for simulation. The baffles were positioned at 0.2 L, 0.4 L, 0.6 L and 0.8 L along the reactor top wall and the roughness elements were located at 0.1 L, 0.3 L, 0.5 L, 0.7 L and 0.9 L respectively on the lower catalyst coated wall. The liquid opening at the baffle tip was 0.33H and the spacing was 0.2 L. Gambits 2.2.30, a meshing tool was employed to generate the grid and quadrilateral cells were utilised to discretise the entire domain of the reactive module with top baffle and roughness elements. A boundary-layer mesh was created at the catalyst coated bottom wall area where the reaction can take place.

Governing equations were solved using the segregated steady-state solver based on control volume technique. Second order upwind discretization method was used, and PRESTO was chosen for the pressure. The pressure-velocity coupling was resolved with SIMPLE algorithm. For accuracy and high convergence of the simulation, the scaled residuals of 10^{-6} for pollutant concentration and 10^{-4} for the continuity and momentum variables was ensured. In addition, a point was chosen in the computational domain where there is high gradient of velocity to monitor the convergence criteria [31,37].

2.3. Boundary condition and grid independence

In this simulation, a no-slip boundary condition was assigned to all walls and baffles surface. The inlet was assigned as velocity-inlet with the inlet velocity of 0.663 m/s, 1.32 m/s, 1.98 m/s and 2.65 m/s normal to inlet surface. The outlet was considered as pressure-outlet boundary conditions at 101,325 Pa (Atmospheric). The hydraulic diameter of outlet and inlet boundary was specified at 15 mm with turbulence intensity (TI) of 5%. A fully developed flow condition was assumed at the outlet. The model was run at constant temperature and properties of the fluid. The summary of the model and the boundary condition considered in this experiment is presented in Table 1.

The accuracy of the numerical solutions mostly relies on the size and number of the cells [39], therefore for the present simulation, the grid dependency test was performed by refining the cell size on the wall and varying channel cell size. To minimise the influence of the quality and size of mesh on the results, preliminary simulations were conducted with the gradual increase of resolution that provides steady results. The best simulation mesh size for various combinations of baffle and roughness elements was determined by changing the mesh size with the constant velocity. At high velocity, the model was simulated with three types of mesh sizes to evaluate the mesh dependency. The three types of meshes considered for the simulation are a coarse mesh of 84,346 elements, a medium mesh of 144,014 elements and a fine mesh of 329,239 elements. The profile of velocity results obtained at 2 mm inside the bottom wall with three mesh sizes are shown in Fig. 3. No significant deviation is observed hence, the number quadrilateral elements for the combined channel was chosen to be 329,239 for subsequent numerical simulation mesh.

3. Results and discussions

This section presents the CFD modelling results obtained with an inlet velocity of 0.15 m/s and 0.5 m/s for the combined top baffle and roughness elements in the reactive section under laminar and turbulent flow regimes. The experimental investigation and CFD modelling were carried out at inlet velocities of 0.663 m/s, 1.32 m/s, 1.98 m/s and 2.65 m/s for validation of CFD model. The fluid flow in an empty reactor without baffles and roughness elements was also simulated for comparison and validation with experimental results.

3.1. Experimental results and model validation

The results from the CFD modelling were validated against the experimental measurements without baffles at different inlet velocities. The experimental investigation and CFD modelling were carried out at inlet velocities of 0.663 m/s, 1.32 m/s, 1.98 m/s and 2.65 m/s and the result obtained is presented in Fig. 4. Fig. 4 shows that the results from both the experiment and simulation are in good agreement. The difference between the experimental and the simulated results were less than 5% which indicate that the developed model can predict the performance of the reactor reasonably accurately.

The model was used to predict the formic acid mass concentration and the results obtained was contrasted with the experimental result. The simulated concentration of formic acid at outlet of the reactor was close to the results obtained experimentally for different

Table 1
Model parameters and boundary conditions.

Model parameters	Condition/Value
Inlet	Velocity
Outlet	Pressure (101,325 Pa)
Wall	No slip
Turbulent intensity	5%
Mesh size	3 mm (84,346 elements), 2 mm (144,014 elements), and 1 mm (329,239 elements)
Fluid	Water (Incompressible and constant properties)

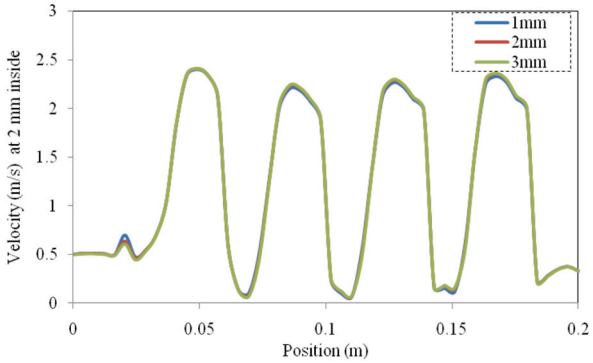

Fig. 3. Simulated result of velocity profile at 2 mm from the reactor bottom of three different meshes used.

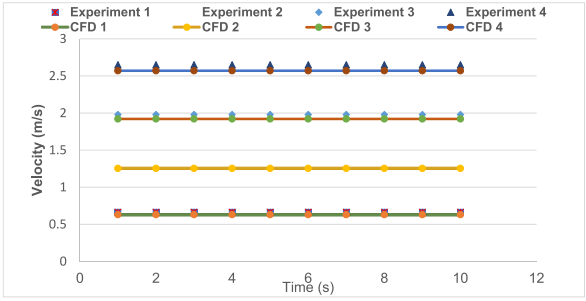

Fig. 4. Experimental and CFD modelling prediction [1].

feed water flow situations as shown in Fig. 5.

3.2. Simulated results of photocatalytic reactor with roughness

3.2.1. Effect of roughness elements on flow

A CFD model of photocatalytic reactor with the semi-circular, triangular, and square shapes roughness with 2.5 mm was developed to examine the influence of bottom wall roughness on the flow field. A reactive section considered for the present simulation was 12 mm in height and 200 mm in length. The simulated results are presented in Fig. 6 which shows the effect of roughness elements on the local streamlines and velocity fields at Reynolds number of 1500 and 7500. The results presented in Fig. 6(a) shows that the addition of roughness elements remarkably perturbs the local flow close to the catalyst coated walls and the inertia causes the detachment tendency.

The rough surfaces have a tendency to generate recirculation at the shadow of the roughness elements when the fluid flows over the triangular and square roughness elements [40]. By assessing the magnitude of the streamline's distortion caused by the types of roughness elements considered, it is evident that the semi-circular roughness element produces smaller distortion area than that of the triangular and square roughness elements. The boundary layer regeneration is normally associated with the recirculation and flow separation caused by the roughness elements. As shown in Fig. 7, the velocity profiles near the bottom wall can provide an in-depth insight of the impacts of roughness on the flow. Most part of the reactive segment has low velocity zones when the Reynold number was

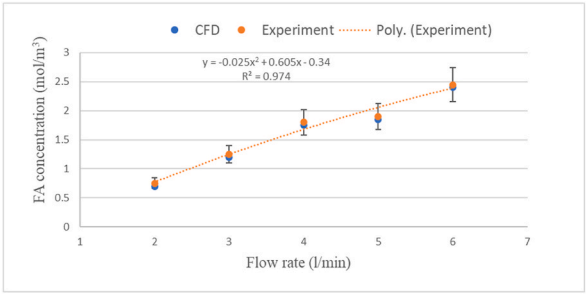

Fig. 5. Comparison of outlet formic acid between experiment and CFD.

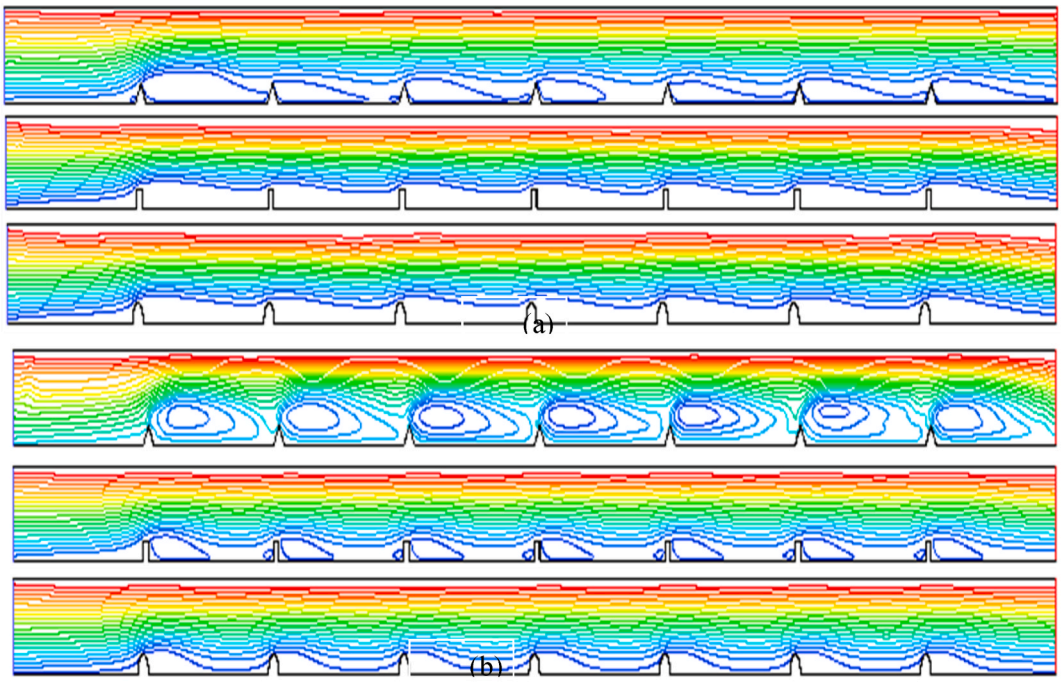

Fig. 6. Effect of roughness on local streamline at (a) Re = 2150 and (b) Re = 7500.

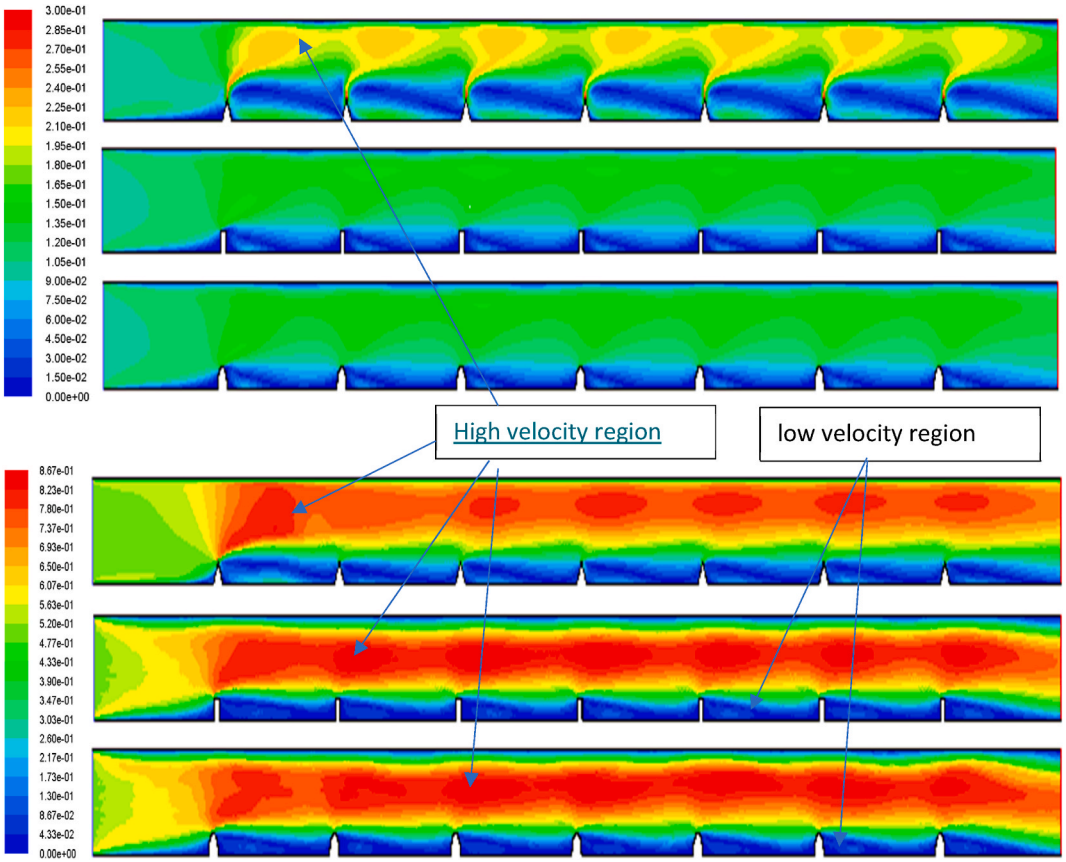

Fig. 7. Effect of roughness on local velocity contours (m/s) at Re = 2150 (top figure) and 7500 (bottom figure) respectively.

2150. At Re = 7500, small area of low velocity of 0.13 m/s exists in the downstream of all roughness elements. Square and triangular elements at Re = 7500 has high alteration of streamlines than that of the semi-circular element. The pressure-drop for triangular roughness and square roughness are same but more than the semicircular roughness features.

3.2.2. Effect of roughness elements on formic acid mass transport

The effect of roughness (square, semi-circle, triangle) on the mass transport of formic acid along the reactive section at Reynolds number 2150 and 7500 is presented in Fig. 8 (a) and (b) respectively. From the figure at Re = 2150, FA concentration at the reactive zone reduces when it moves toward the outlet of the domain for all the elements investigated. The figure also shows that the FA mass fraction at the photocatalyst surface reduces considerably for the square element as compared with other elements for the conditions simulated. The inlet FA mass fraction was 3.40×10^{-3} and the average mass fraction at the outlet was found to be 2.55×10^{-3}, 2.30×10^{-3}, and 2.3×10^{-3} at Re = 2150 for rectangular, triangular and semi-circular roughness elements whereas at Re = 7500, no significant change was observed. The lower concentration of FA prevails over 50% of the reactive area for triangle and semicircle elements. This phenomenon could be attributed to the velocity condition in the domain which demonstrated a recirculation zone at some locations that stimulates high velocity gradient areas across the flow. In contrast, a low FA mass concentration was found for the semi-circular and square elements compared to that ascribed to the triangular element at Re = 7500. The degradation of FA was approximately 25%, 32.5% and 32.5% when rectangular, triangular, and semi-circular roughness was used respectively. When baffle and roughness was used combinedly, the degradation of FA was approximately 35%, 37% and 32% when rectangular, triangular, and semi-circular roughness was used respectively. The higher velocity gradients in these zones causes the higher concentration zones [41]. Relatively the extent of the low concentration area is significantly smaller at turbulent flow than in laminar flow.

3.3. Simulated results of photocatalytic reactor with top baffle and roughness

3.3.1. Effect of top baffle and roughness elements on turbulence wall shear stress and pressure drop

The results of wall shear obtained from the simulation for high and low Reynolds number is presented in Fig. 9. The results show that the wall shear stress fluctuates along the flow for all element of baffles and roughness studied except empty one which does not show any variation. Higher wall shear stress was found at the 0.2 m, 0.3 m, 0.6 m, and 0.8 m from the inlet of reactor for square and triangular roughness elements when fluid move toward the reactor exit. For the semi-circular element, the high shear stress at the wall were observed to be at the positions of 0.05 m, 0.08 m, 0.12 m, and 0.16 m respectively from the inlet. The simulation results indicate that the distribution of wall shear stress is maximum in the middle of the successive roughness elements and minimum at the position of the roughness element for any rate of turbulent flow. At low Reynolds number, the higher shear stress 5.0 Pa is achieved with square and triangular elements which extend over the maximum length of the reactive section. By contrast the higher wall shear stress for the

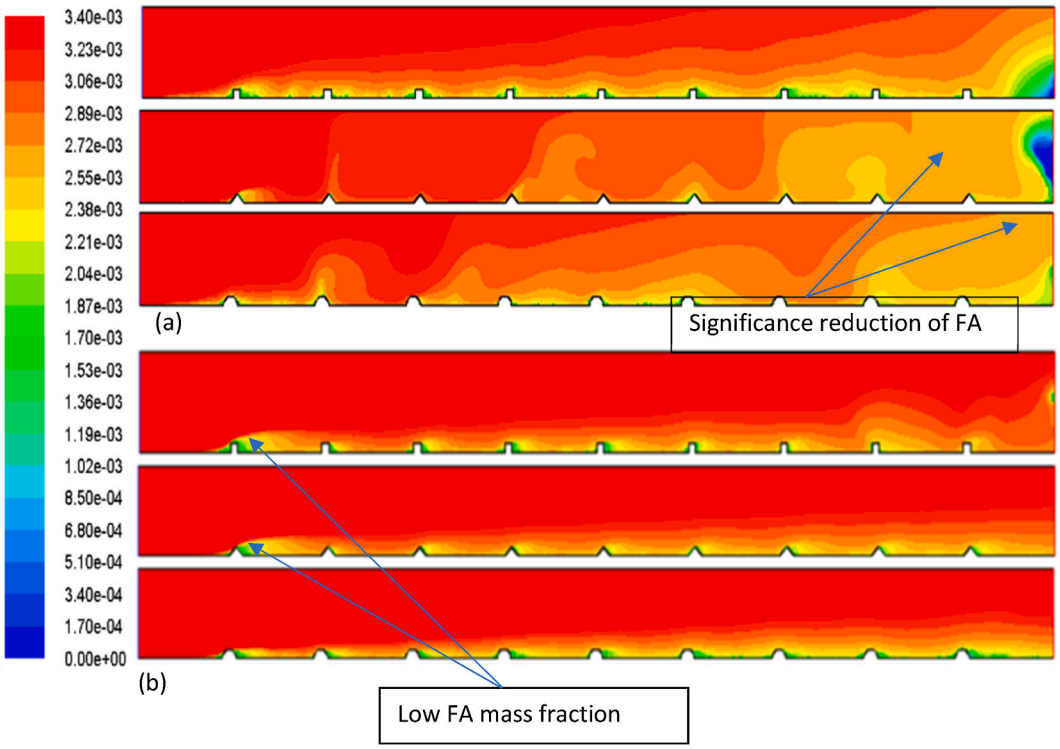

Fig. 8. Effect of roughness on FA mass fraction at (a) Re = 2150 and(b) Re = 7500.

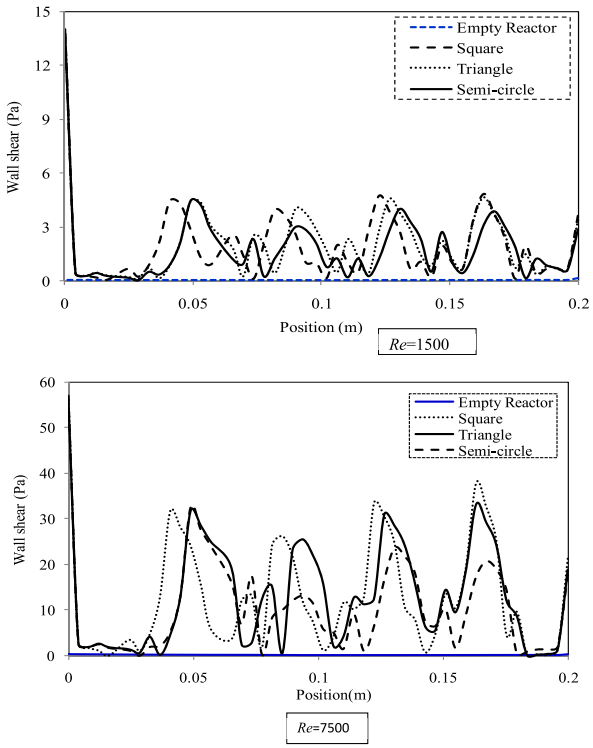

Fig. 9. Effect of combined baffle and roughness elements on the wall shear stress distribution on the catalyst coated surface.

semi-circular element ranges from 2.8 to 4.5 Pa. At high Reynolds number, the maximum shear stress obtained using the square and triangular elements was 25–35 Pa which stretches for the larger part of the reactive section. On the contrary, the higher wall shear stress varies from 10 to 32 Pa for the semi-circular element at higher Reynold number. In comparison with the empty reactor, the application of combined baffles and roughness elements would also lead to significant increase in the friction factor. Two minimum friction force may be present due to the flow separation through the baffle; first one is around the baffle and the second one behind the baffle at the reattachment point.

The turbulence kinetic energy (TKE) distribution along the reactive length is shown in Fig. 10. The existence of baffles and roughness components along the flow produces the repeated variation in flow direction and the quick velocity variation, which produces high turbulence. It can be found that the magnitude of TKE is lower at the upstream of the first top baffle position than in the remaining section for both low and high Reynolds numbers. A strip of low TKE region exist downstream of each top baffle position irrespective of the fluid flow rate through the combined reactive module. At low Reynolds number flow rate, the higher values of TKE appear at the right side of the roughness element top for all the cases studied. In contrast to the smooth reactive section, the use of combined baffle and roughness elements in the reactive section generates high TKE, which implies that the flow in the combined baffled reactive zone is totally turbulent. The fluid remains highly turbulent in the entire domain and can change the concentration boundary layer significantly and reduce the accumulation of pollutant and its degradation products on the catalyst coated surface. Nevertheless, the local energy dissipation rate will be higher as well, that may add to the pressure drop in the reactive area because of the turbulent energy dissipation. Duran et al. [32] suggested that the increase in turbulence intensity has substantial effect on improving the contaminant degradation rate in an immobilized photocatalytic reactor. To elucidate the impact of turbulence intensity on the contaminant mass transfer rate, the CFD simulated turbulence intensity in the plain reactor and that of the reactor equipped with the square, triangular and semicircular roughness elements are investigated. Further, the difference of turbulence intensity simulated at Re = 7500 all over the reactive section was compared with an empty reactive section. The predicted turbulence intensity fields were different for the reactor equipped with the baffle and roughness element compared with the empty reactive module. The simulation results indicate a significant difference between the turbulence intensities close to the wall and the middle of the reactive module.

At Re = 2150, the maximum turbulent kinetic energy (TKE) was observed to be 4.43×10^{-2}, 3.25×10^{-2} and 2.66×10^{-2} for rectangular, triangular, and semi-circle roughness element. At Re = 7500, the maximum TKE was observed to be 4.77×10^{-2} behind the second roughness element for all types considered. The use of top baffle and roughness elements inside the reactor shows the pattern of turbulence intensity and it is found that the area near the bottom wall has higher intensities due to the sharp edges of the top baffle. While the swirling flow pattern created by the semi-circular element was somewhat lower than that achieved with the square and triangular elements. The enhanced fluid mixing and turbulence intensity as well as the fluid vorticity at the back of the square and triangular edges exceeded the negative impacts of weakened swirls on mass transfer augmentation. This is crucial from contaminant

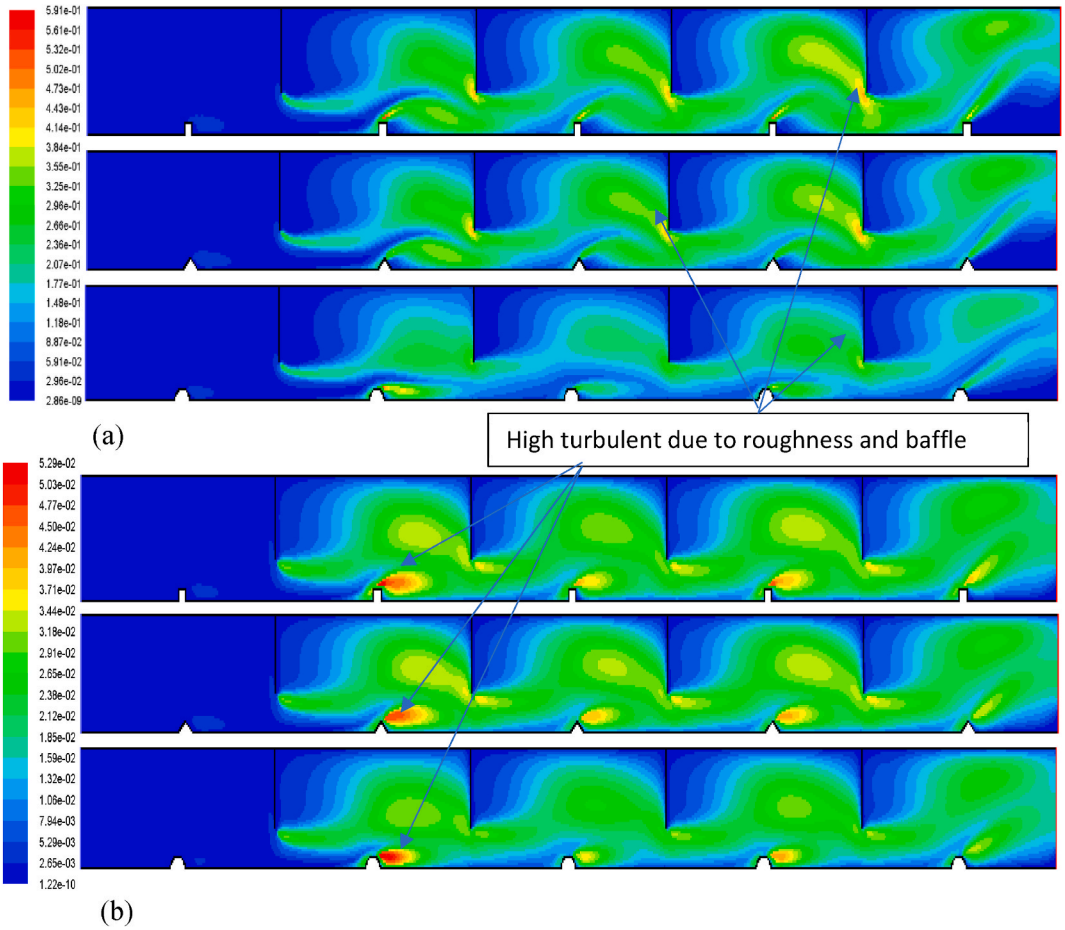

Fig. 10. Effect of combined baffle and roughness elements on turbulent kinetic energy (m^2/s^2) along the reactive section for (a) Re = 2150 and (b) Re = 7500 respectively.

mass transfer point of view, and this may imply why more species mass fraction is transferred by the combined baffle and roughness system than that was observed for the roughness element only. The higher turbulence intensity near to the reactor wall has been appeared as one of the reasons that the highest TKE obtained by the square element insert.

Fig. 11 shows the change of static pressure in the reactive module for both Re = 2150 and 7500 respectively. In general, the increase of turbulence is combined with the loss of increased skin friction which causes in higher pressure-drop. Pressure-drop is a phenomenon that can't be avoided in a baffle-filled reactive channel. The amount of pressure-drop in a reactive channel containing baffles is dominated by the baffle shapes and the flow rates of fluid. Different types of roughness element combined with a top baffle can result in

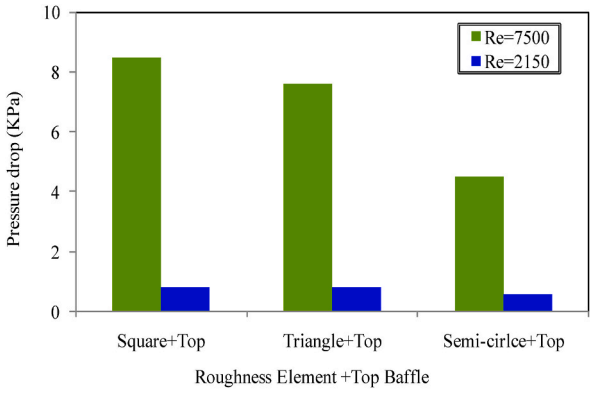

Fig. 11. Effect of combined top baffle and roughness elements on pressure drop.

different degrees of pressure-drop in the reactive channel under the simulation conditions. The square elements which produce the highest velocity at the lower section of the reactive section resulted in the highest pressure-drop followed by triangular and circular elements.

It was observed that the static pressure reduced quickly for a distance from 0.8 L to the reactor exit for the square and triangular elements. The liquid is pushed through the constricted zone and then expands after the top-baffle position to fill up the channel. This periodic expansion and contraction in the flow area increase the fluid velocity which subsequently affects the eddy formation. This phenomenon directly increases to the pressure-drop in this restricted channel. At high Reynolds number, higher unsteady hydrodynamics grow which causes the square element to produce a higher pressure drop when compared with triangular and semicircular elements [42]. With increasing Reynolds number, the variation in pressure drop caused by various combined reactor configurations becomes more obvious. The triangular and square elements create relatively higher-pressure drop followed by the semi-circular roughness element at Re = 2150. Moreover, present modelling methods generates different trends as compared to the reactor system equipped with only a top baffle (triangular elements generate the highest pressure-drop followed by the square and semi-circular elements) at higher Reynolds number.

3.3.2. *Comparative evaluation of significant hydrodynamic parameters*

To assess the effect of combined top baffle and roughness elements on the hydrodynamic performance of the reactive module, several parameters that are hydro-dynamically important were compared for both low and high Reynolds number flows. Table 2 shows the maximum, minimum and average values of hydrodynamic parameters simulated with an inlet velocity of 0.15 m/s and 0.5 m/s for the square, triangular and semi-circular roughness elements respectively. Table 3 present the maximum, minimum and average values of hydrodynamic parameters simulated with an inlet velocity of 0.15 m/s and 0.5 m/s for the combined top baffle and roughness elements. The computed pressure-drop, turbulent kinetic energy, wall shear stress and turbulent energy dissipation rate for the square, triangle and semi-circular elements are summarised in Table 2 and Table 3for both low and high Reynolds number respectively. In terms of pressure drop, the top baffle and semi-circular system seems to be more realistic compared to the square and triangle elements for both cases. In addition, the semi-circular element also seems to be more efficient with respect to the amount of % contact loss. Therefore, it can be suggested that the top baffle combined with a semi-circular element would provide optimum hydrodynamic performance with minimal pressure-drop and energy consumption for both low and high Reynolds number flows.

In contrast to the boundary layers that formed in the reactive section with only square, triangular, and semi-circular roughness elements, there is a gradual increase of the separation of the boundary layers in the combined reactive module which increases the creation of vortices in the flow, thereby improving the extent of mixing. The generated vortices tend to split up the streams into multiple layers which curl in a different manner. The combination of splitting, curling, and the co-mingling of the centre streamlines and the edge streamlines will lead to enhanced mixing and will enhance the performance of the reactor. In contrast, the smooth channel or the channel with only roughness elements does not have this advantage. In the combined top baffle and roughness element part, the fluid passing through the reactive channel is rotated as expected. Some variations are found that could result from the variation in laminar and turbulent flows. At higher Reynolds number, fluid molecules were extensively mixed, and the interface of fluid molecules became more distorted. As the fluid passes through the combined reactive section with a helically rotational shape, the fluid molecules are elongated and folded because of inertial force. This convection can widen the area of interface, which starts fast mixing of fluid particles at a higher Reynolds number. Reynolds number plays a crucial role in analysing the flow field. The degree of mixing arising specially from the diffusion under pure laminar flow conditions reduced rapidly with increasing velocity, as the residence time is decreased within the channel. As the Reynolds number becomes larger, recirculation arises in the flow of the combined reactive section, the streamline becomes unsymmetrical, and the pressure in the channel undergoes a series of changes as well.

3.3.3. *Combined top baffle and roughness elements on the velocity and mass flow of formic acid*

All three roughness elements mentioned earlier were selected for simulation to explore the influence of bottom wall roughness on the flow phenomena. Fig. 12 presents the effect of top baffles combined with the semi-circular, triangular, and square roughness elements on the local streamlines and velocity fields at Re = 2150 and 7500 respectively. The predicted flow pattern for various configurations seems to be similar except for flow zones close to the roughness. As presented in Fig. 12, the use of roughness on the

Table 2
Effect of roughness elements on hydrodynamic parameters.

Parameter		Inlet velocity = 0.15 m/s (Re = 2150)			Inlet velocity = 0.5 m/s (Re = 7500)		
		Square	Triangle	Semi-circle	Square	Triangle	Semi-circle
Pressure-drop (KPa)		0	0	0	0	0	0
Turbulent kinetic energy (m^2/S^2)	*Max.*	2.44×10^{-3}	0.39	1.92×10^{-3}	2.7×10^{-2}	0.426	2.08×10^{-2}
	Min.	4.53×10^{-11}	8.17×10^{-11}	3.48×10^{-11}	1.18×10^{-8}	1.1×10^{-8}	1.21×10^{-10}
Wall shear,τ_w (Pa)	*Max.*	2	3.5	2.0	8	10	7
	Min.	0	0	0	0	0	0
	Avg.	1	1.15	0.85	5	7	5
Turbulent dissipation rate (m^2/S^3)	*Max.*	1×10^{-3}	4×10^{3}	2.5×10^{-2}	0.6	2×10^{3}	0.4
	Min.	1×10^{-2}	1×10^{-4}	1×10^{-3}	1×10^{-2}	1×10^{-4}	1×10^{-3}
% Contact loss		87.5	87.5	43.75	81.25	85.0	81.25

Table 3
Effect of combined top baffle and roughness elements on hydrodynamic parameters.

Parameter		Inlet velocity = 0.15 m/s (Re = 2150)			Inlet velocity = 0.5 m/s (Re = 7500)		
		Square	Triangle	Semi-circle	Square	Triangle	Semi-circle
Pressure drop (KPa)		0.8	0.75	0.65	8	7.5	5.2
Turbulent kinetic energy (m^2/S^2)	*Max.*	4×10^{-5}	2.5×10^{-5}	0.5×10^{-6}	0.394	0.4	0.414
	Min.	1×10^{-5}	1×10^{-6}	5×10^{-6}	3.32×10^{-9}	3.08×10^{-9}	2.86×10^{-9}
Wall shear,τ_w (Pa)	*Max.*	5.0	5.0	5.0	40.0	40.0	39.0
	Min.	0	0	0	0	0	0
	Avg.	2.5	1.75	2	20	18	17.5
Turbulent dissipation rate (m^2/S^3)	*Max.*	6	3	0.5	100	50	48
	Min.	0.25	0.25	1.0	0	0	0
% Contact loss		35	34	20	40	40	30

catalyst coated layer obviously disrupts the flow near the walls which results in a detachment tendency due to inertia.

When the fluid flows over the square, semicircular, and triangular roughness elements, the flow due to rough surfaces tend to stimulate recirculation at the back of the roughness elements. The streamlines distortion caused by semicircle roughness element is smaller than that of the triangular and square roughness elements at high Reynolds number. The regeneration of the boundary layer typically relies on the flow separation and recirculation due to the roughness elements [40]. The boundary layer regeneration is one of the main causes for the enhancement of the flow separation and convective mass transfer and the recirculation can be linked with the increase in pressure drop. A large recirculation or a central vortex is found to be created at the top of the roughness elements for both low and high flow rates. The central recirculation zone tends to expand between the inter-baffle region irrespective of the roughness elements. At low *Re*, the vortices formed behind the triangular and semi-circular roughness elements seem to be larger compared with that of the square element. However, the size of the vortex behind the semi-circular element is somewhat smaller than that produced with the square and triangular elements at high Reynolds number. The central recirculation zone thus formed between the top baffle results in the fluid to rotate with a strong motion which may cause the fluid near baffle and the wall to flow in the main region. It is observed that the largest vortex is just situated at mid positions between the successive top baffles. The size of the central recirculation area is larger as compared with the ones that produced in square and triangular roughness elements at the corner. It can be concluded that the addition of the baffle creates longer flow path with a strong vortex because of the change in its orientation.

Fig. 13 presents the contours of velocity along the reactive zone at Reynolds numbers 2150 and 7500 respectively. The velocity

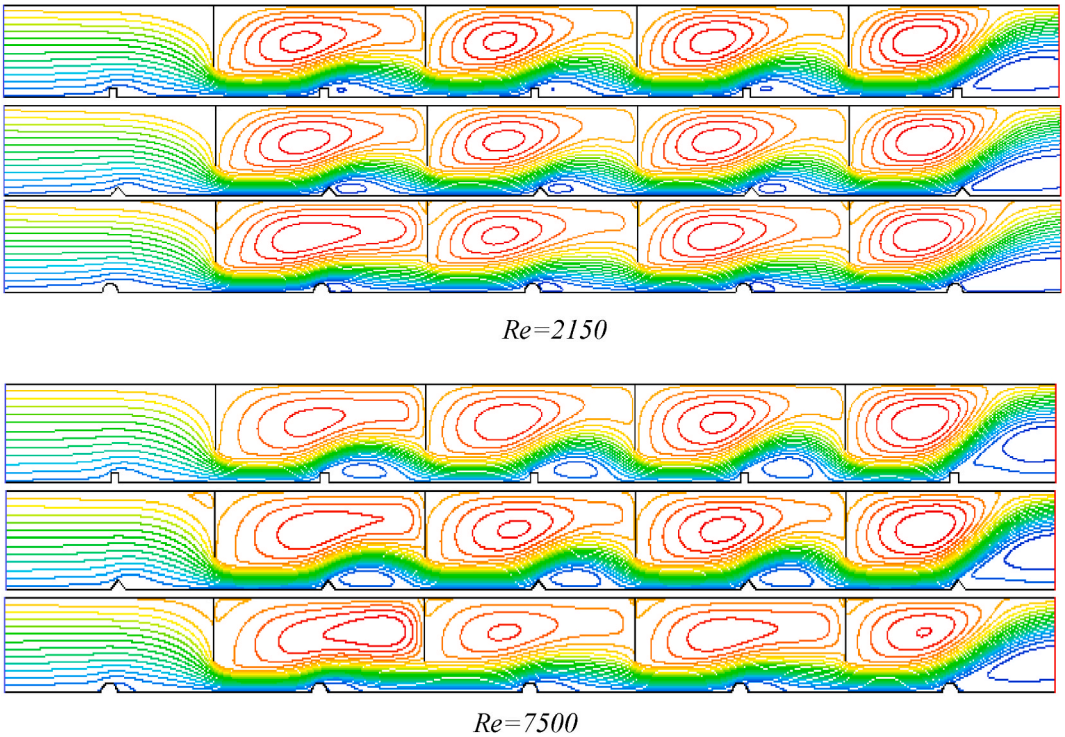

Fig. 12. Contours of local streamlines obtained with combined top baffle and semi-circular, triangular, and square elements for Re = 2150 (top) and 7500 (bottom) respectively.

distribution close to the bottom wall can provide some insight about the role of roughness elements on the fluid flow. At Re = 2150, the low velocity region seems to dominate a major part of the reactive zone. On the contrary, for Re = 7500 a low velocity strip of 0.15 m/s to 0.27 m/s exists downstream of the triangular and square elements but the extent of the low velocity region is small for the semi-circular element. The distortion of streamlines at Re = 7500, over the triangular and square elements are higher compared with the semi-circular element. The impact of triangular elements on pressure-drop along the reactor surface was similar to the square roughness elements, and their effect is higher than the semicircular roughness element. The flow produced by this combined arrangement appears to be helical in pattern which flows along the channel and generates secondary flow to combat the formation of deposited layer immediately above the catalyst TiO_2 coated surface. This flow results in helical flow vortices which create fluid instabilities in the reactive medium and thus inevitably scarps the surface of the photocatalyst. The vortices formed by the settings are anticipated to perform better by enhancing the mixing between the boundary layer and the bulk fluid to a larger extent than that happens by only using the reactor with and without roughness elements.

The combined reactor will produce dispersion and spreading of mixed fluids that lead to further turbulent collisions, and lower pressure drops than that of the smooth and top baffle reactors. The flow varies all over the reactive section for all the cases at both Re = 2150 and 7500 respectively. Under the conditions studied, the magnitudes of highest velocity seem to persist at the channel bottom for all configurations. In contrast velocities with lower magnitudes prevail in the inter-baffle regions in the upper portion of the reactive zone. The laminar flow was observed to become entirely unstable at the higher Reynolds number [43] and the instability threshold would be the flow at Re around 2150. In general, as the fluid flow past the sharp turns, a transverse secondary flow to the primary flow is formed [43]. As a result, the presence of the top baffles and roughness elements in the reactive section can lead to the formation of vortices. This makes the mean flow velocity comparatively low, and thus, contributes to enlarging the residence time of the flow, in the reactive channels. This periodical back flow results in a pressure gradient opposite to the flow, which might be related to the lower pressure drop across the combined reactor compared with the top baffle and plain reactor.

To ensure a rapid and effective mixing, the design of a photocatalytic reactor is an essential step. In the laminar flow regime, the mixing of fluids in a reactor is mainly driven by the diffusion process. Under the laminar flow condition, the mixing of fluid requires a long enough path and wide space to ensure complete mixing or a complex geometry to raise, stretch, and tilt the fluid interfaces to ensure complete mixing based on chaotic advection. But in areas where the turbulence is high, the lifetime of eddy, k/ε, is short, mixing is quick, and, consequently, the rate of reaction may not be constrained by the small-scale mixing. In this constraint, the kinetic rate generally has the smallest value [44]. In contrast, in areas with low turbulence levels, small-scale mixing may be slow and reduce the reaction rate. In this range, the mixing rates are more significant. When the mixing in the reactive section is efficient, diffusion activities are significantly accelerated; organic pollutant close to the wall goes into the bulk and vice versa, thereby removing a slowdown due to weakening concentration gradients.

Fig. 14 shows a comparison between the contours of formic acid concentration along the reactive zone at Reynolds number 2150 (top) and 7500 (bottom) under the impact of roughness elements such as semi-circle, triangle, and square respectively. The inlet FA mass fraction was 3.40×10^{-3} and the average mass fraction at the outlet was found to be 2.21×10^{-3}, 2.15×10^{-3}, and 2.32×10^{-3} at Re = 2150 for rectangular, triangular and semi-circular roughness elements whereas at Re = 7500, the average mass fraction at the outlet was found to be 2.11×10^{-3}, 2.15×10^{-3}, and 2.20×10^{-3} for rectangular, triangular and semi-circular roughness elements. For Re = 2150, figure shows that the FA concentration across the reactive zone varies significantly as the flow passes the channels and approaches the exit in both cases for all the roughness elements examined. For the current simulation condition, the concentration of FA at the shadow of square and triangular elements on the photocatalyst surface reduces significantly as compared with the semi-circular roughness. The low FA concentration appears to spread over the 50% span of the reactive zone. This situation was confirmed through assessment of the velocity in the domain which revealed a recirculation area at the upstream and downstream of the triangular and square elements in the inter-baffle region that generates high velocity gradient. By contrast, at Re = 7500, a low FA concentration present at the shadow of semi-circular, triangular, and square elements compared to that ascribed to the case with Re = 2150. These high concentration areas are the outcome of higher velocity gradients in this region [41]. Relatively the scale of the low concentration area is noticeably smaller in turbulent flow than that in laminar flow. The reactor top and bottom wall featured with top baffles and roughness elements respectively generates dispersion and spreading of mixed fluids that leads to more turbulent collisions than plain straight channels. The main difference between plain and the combined reactor can be clarified by the fact that staggered obstacle feature walls in the combined channel force the fluid particles near the walls to co-mingle with the fluid particles in the middle of the channel which is also the reason for the better mixing efficiency.

4. Conclusions

In this study, a CFD model has been created and numerical modelling has been carried out to examine the hydrodynamic performance of photocatalytic reactor with baffle and roughness. The baffles were placed at the top of the wall and the roughness element were place at the bottom wall of the reactive area. ANSYS FLUENT software was used to simulate the model with two different flow rates to study the role of fluid dynamics in the photocatalytic reactor at Reynolds numbers 2150 and 7500 respectively. The results from the simulation show that the baffles and roughness element enhance the hydrodynamics performance. Based on the analysis and comparison it is evident that the combined reactor appears to be a more promising approach in terms of turbulence and pressure drop at low flow regimes which needs further investigation to determine its optimum residence time, turbulence phenomena, and better mixing than that of the others. The combined baffles and roughness generate turbulence that enhance the mixing which will help degradation of the pollutant. The results from the simulation were validated against the experimental data which show good

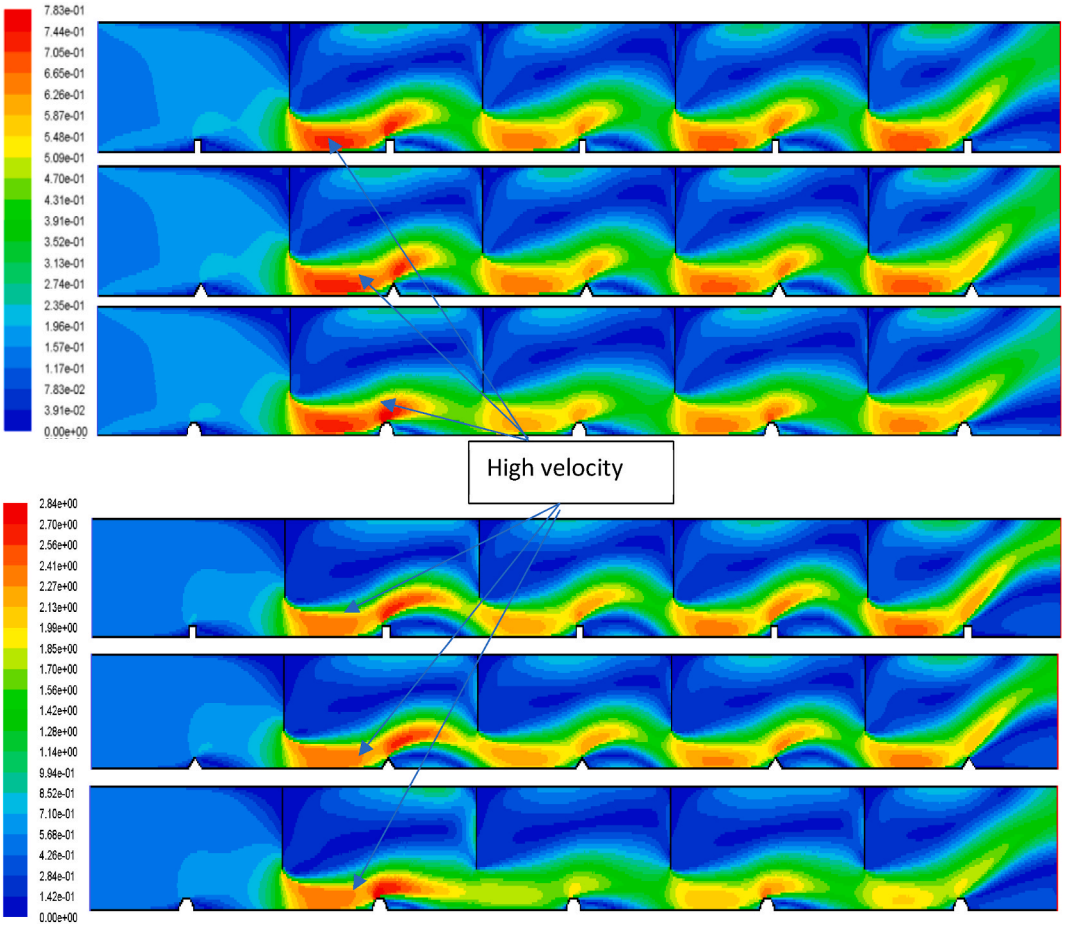

Fig. 13. Contours of velocity field for Re = 2150 (top) and 7500 (bottom) respectively.

agreement, variation within 5%, therefore the model can be used to predict the flow phenomena and pollutant degradation. The simulation result shows that the addition of baffles and roughness on the reactive surfaces increases the turbulent kinetic energy (minimum increase 8%) and consequently increases the mass transfer (maximum increase 37%) of the pollutant. The highest shear was observed to be 40 kPa during the CFD modelling when square and triangular elements were employed. The highest-pressure-drop of 8 kPa was found when the square element was used during the CFD modelling. The FA degradation was higher when both baffles and roughness used combinedly compared to when only baffles were used. The degradation of FA was found to be approximately 35%, 37% and 32% when rectangular, triangular and semi-circular roughness was used combinedly. Overall, the photocatalytic reactor performance is significantly enhanced by the application of combined baffles and roughness elements in the reactive surface.

Author contributions

All authors have read the manuscript and agreed to publish the manuscript. The contributions of each author are outlined below: M.G. Rasul: Conceived and designed the experiment. S. Ahmed: Performed the experiments; analysed and interpretated the data. M. A. Sattar: Wrote the paper; analysed and interpretated the data. M.I. Jahirul: Contributed reagent, materials, analysis tools; Wrote the paper.

Data availability statement

Data will be made available on request.

Declaration of competing interest

The authors declare that they have no known competing financial interests or personal relationships that could have appeared to influence the work reported in this paper

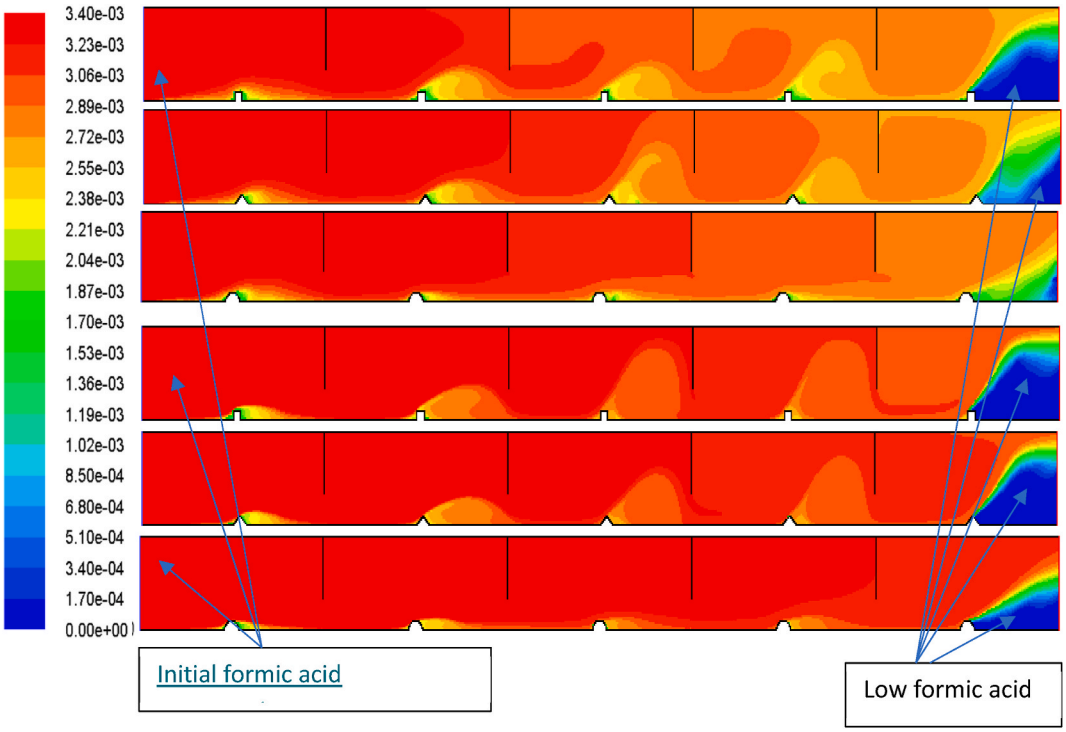

Fig. 14. Contours mass fraction of formic acid as computed at Re = 2150 (top figure) and 7500 (bottom figure) respectively.

References

[1] S. Ahmed, M.G. Rasul, M.A. Sattar, M.I. Jahirul, Phenol degradation of waste and stormwater on a flat plate photocatalytic reactor with TiO2 on glass slide: an experimental and modelling investigation, J. Water Proc. Eng. 47 (2022), 102769.

[2] M.C. Tomei, D. Mosca Angelucci, E. Clagnan, L. Brusetti, Anaerobic biodegradation of phenol in wastewater treatment: achievements and limits, Appl. Microbiol. Biotechnol. 105 (6) (2021) 2195–2224.

[3] R. Binjhade, R. Mondal, S. Mondal, Continuous photocatalytic reactor: critical review on the design and performance, J. Environ. Chem. Eng. 30 (2022), 107746.

[4] M. Janczarek, E. Kowalska, Computer simulations of photocatalytic reactors, Catalysts 11 (2) (2021) 198.

[5] E. Tetteh, S. Rathilal, D. Naidoo, Photocatalytic degradation of oily waste and phenol from a local South Africa oil refinery wastewater using response methodology, Sci. Rep. 10 (1) (2020) 1–12.

[6] Z. Wang, C. Li, K. Domen, Recent developments in heterogeneous photocatalysts for solar-driven overall water splitting, Chem. Soc. Rev. 48 (7) (2019) 2109–2125.

[7] A.A. Ismail, D.W. Bahnemann, Photochemical splitting of water for hydrogen production by photocatalysis: a review, Sol. Energy Mater. Sol. Cell. 128 (2014) 85–101.

[8] K.P. Sundar, S. Kanmani, Progression of Photocatalytic reactors and it's comparison: a Review, Chem. Eng. Res. Des. 154 (2020) 135–150.

[9] A.A. Adesina, Industrial exploitation of photocatalysis: progress, perspectives and prospects, Catal. Surv. Asia 8 (4) (2004) 265–273.

[10] J.M. Herrmann, Heterogeneous photocatalysis: state of the art and present applications, Catalysis 34 (1) (2005) 49–65.

[11] R. Molinari, M. Mungari, E. Drioli, A. Di Paola, V. Loddo, L. Palmisano, M. Schiavello, Study on a photocatalytic membrane reactor for water purification, Catal. Today 55 (1) (2000) 71–78.

[12] K. Sopajaree, S.A. Qasim, S. Basak, K. Rajeshwar, An integrated flow reactor-membrane filtration system for heterogeneous photocatalysis. Part I: experiments and modelling of a batch-recirculated photoreactor, J. Appl. Electrochem. 29 (5) (1999) 533–539.

[13] S. Ahmed, M.G. Rasul, R. Brown, M.A. Hashib, Influence of parameters on the heterogeneous photocatalytic degradation of pesticides and phenolic contaminants in wastewater: a short review, J. Environ. Manag. 92 (3) (2011) 311–330.

[14] S. Ahmed, M.G. Rasul, W.N. Martens, R. Brown, M.A. Hashib, Heterogeneous photocatalytic degradation of phenols in wastewater: a review on current status and developments, Desalination 261 (1) (2010) 3–18.

[15] D. Wu, X. Wang, Y. An, X. Song, N. Liu, H. Wang, Z. Gao, F. Xu, K. Jiang, Hierarchical TiO2 Structures Derived from F− Mediated Oriented Assembly as Triple-functional Photoanode Material for Improved Performances in CdS/CdSe Sensitized Solar Cells, Electrochim. Acta 248 (2017) 79–89.

[16] H. Wang, D. Wu, W. Wu, D. Wang, Z. Gao, F. Xu, K. Cao, K. Jiang, Preparation of TiO2 microspheres with tunable pore and chamber size for fast gaseous diffusion in photoreduction of CO2 under simulated sunlight, J. Colloid Interface Sci. 539 (2019) 194–202.

[17] P.S. Saud, B. Pant, A.P. Twari, Z.K. Ghouri, M. Park, H.-Y. Kim, Effective photocatalytic efficacy of hydrothermally synthesized silver phosphate decorated titanium dioxide nanocomposite fibers, J. Colloid Interface Sci. 465 (2016) 225–232.

[18] H. Aliyeva, A. Gurel, S. Nowak, S. Lau, P. Decorse, S. Chaguetmi, D. Schaming, S. Ammar, Photo-anodes based on TiO2 and carbon dots for photo-electrocatalytical measurements, Mater. Lett. 250 (2019) 119–122.

[19] T. Rathna, J. PonnanEttiyappan, R. D, Fabrication of visible-light assisted TiO2-WO3-PANI membrane for effective reduction of chromium (VI) in photocatalytic membrane reactor, Environ. Technol. Innovat. 24 (2021), 102023.

[20] Z.-k. Zhuang, Z.-m. Yang, S.-y. Zhou, H.-q. Wang, C.-l. Sun, Z.-b. Wu, Synergistic photocatalytic oxidation and adsorption of elemental mercury by carbon modified titanium dioxide nanotubes under visible light LED irradiation, Chem. Eng. J. 253 (2014) 16–23.

[21] C.C. Pei, W.W.-F. Leung, Photocatalytic oxidation of nitrogen monoxide and o-xylene by TiO2/ZnO/Bi2O3 nanofibers: optimization, kinetic modeling and mechanisms, Appl. Catal. B Environ. 174–175 (2015) 515–525.

[22] S. Riaz, S.-J. Park, An overview of TiO2-based photocatalytic membrane reactors for water and wastewater treatments, J. Ind. Eng. Chem. 84 (2020) 23–41.

[23] M. Jafarikojour, B. Dabir, M. Sohrabi, S.J. Royaee, Application of a new immobilized impinging jet stream reactor for photocatalytic degradation of phenol: reactor evaluation and kinetic modelling, J. Photochem. Photobiol. Chem. 364 (2018) 613–624.
[24] J. Bai, R. Wang, Y. Li, Y. Tang, Q. Zeng, L. Xia, X. Li, J. Li, C. Li, B. Zhou, A solar light driven dual photoelectrode photocatalytic fuel cell (PFC) for simultaneous wastewater treatment and electricity generation, J. Hazard Mater. 311 (2016) 51–62.
[25] M. Tahir, B. Tahir, Z.Y. Zakaria, A. Muhammad, Enhanced photocatalytic carbon dioxide reforming of methane to fuels over nickel and montmorillonite supported TiO2 nanocomposite under UV-light using monolith photoreactor, J. Clean. Prod. 213 (2019) 451–461.
[26] L. Hurtado, E. Torres-García, R. Romero, A. Ramírez-Serrano, J. Wood, R. Natividad, Photocatalytic performance of Li1−xAgxVMoO6 (0⩽x⩽1) compounds, Chem. Eng. J. 234 (2013) 327–337.
[27] S. Ahmed, M.G. Rasul, W.N. Martens, R. Brown, M.A. Hashib, *Advances in heterogeneous photocatalytic Degradation of Phenols and Dyes in wastewater: a review.* Water, air, & Soil Pollution 215 (1) (2011) 3–29.
[28] M.G. Rasul, S. Ahmed, M.A. Sattar, M.I. Jahirul, Modelling and analysis of hydrodynamics and flow phenomena of fluid with formic acid as pollutant in the reactive area of a flat plate photocatalytic reactor with top and bottom turbulence promote, Chem. Eng. J. 466 (2023), 142760.
[29] S. Sripattanapipat, P. Promvonge, Numerical analysis of laminar heat transfer in a channel with diamond-shaped baffles, Int. Commun. Heat Mass Tran. 36 (1) (2009) 32–38.
[30] M.F. Kabir, A.K. Ray, Performance enhancement of a chemical reactor utilizing flow instability 78 (2–3) (2003) 314–320.
[31] J. Esteban Duran, F. Taghipour, M. Mohseni, CFD modeling of mass transfer in annular reactors, Int. J. Heat Mass Tran. 52 (23) (2009) 5390–5401.
[32] J.E. Duran, M. Mohseni, F. Taghipour, Computational fluid dynamics modeling of immobilized photocatalytic reactors for water treatment, AIChE 57 (7) (2011) 1860–1872.
[33] J.O.d.B. Lira, H.G. Riella, N. Padoin, C. Soares, Fluid dynamics and mass transfer in curved reactors: a CFD study on Dean flow effects, J. Environ. Chem. Eng. 10 (5) (2022), 108304.
[34] R. Peralta Muniz Moreira, G. Li Puma, Multiphysics computational fluid-dynamics (CFD) modeling of annular photocatalytic reactors by the Discrete Ordinates method (DOM) and the six-flux model (SFM) and evaluation of the contaminant intrinsic kinetics constants, Catal. Today 361 (2021) 77–84.
[35] B. Deng, Y. Jiang, L. Gao, B. Zhao, CFD Modeling of Ethylene Degradation in Gas-phase Photocatalytic Reactors, Environmental Science and Pollution Research, 2022.
[36] Fluent-Inc, FLUENT 6.3 User's Guide. Modelling Turbulence, Fluent-Inc., Lebanon, NH, 2006.
[37] J.E. Duran, M. Mohseni, F. Taghipour, Modeling of annular reactors with surface reaction using computational fluid dynamics (CFD), Chem. Eng. Sci. 65 (3) (2010) 1201–1211.
[38] V. Ranade, Computational Flow Modelling for Chemical Reactor Engineering, Academic Press, London, 2002.
[39] H.K. Versteeg, W. Malalasekera, An Introduction to Computational Fluid Dynamics: the Finite Volume Method, Pearson education, 2007.
[40] C. Zhang, Y. Chen, M. Shi, Effects of roughness elements on laminar flow and heat transfer in microchannels, Chem. Eng. Process: Process Intensif. 49 (11) (2010) 1188–1192.
[41] J.E. Duran, F. Taghipour, M. Mohseni, Evaluation of model parameters for simulating TiO2 coated UV reactors, Water Sci. Technol. 63 (7) (2011) 1366–1372.
[42] J.E. Duran, M. Mohseni, F. Taghipour, Computational fluid dynamics modeling of immobilized photocatalytic reactors for water treatment 57 (7) (2011) 1860–1872.
[43] A. Jarandehei, A. De Visscher, Three-dimensional CFD model for a flat plate photocatalytic reactor: degradation of TCE in a serpentine flow field, AIChE 55 (2) (2009) 312–320.
[44] E.M. Marshall, A. Bakker, Computational fluid mixing, in: Handbook of Industrial Mixing, 2003, pp. 257–343.